Electronic Supplementary Information (ESI)

Unexpected Room Temperature Phosphorescence from Non-aromatic Pure Organic Molecule with low molecular weight of 85: How the Intermolecular Hydrogen Bond Creates Wonderful Flash

Manman Fang,[a] Jie Yang,[a] Xueqin Xiang,[b] Yujun Xie,[a] Yongqiang Dong,[b] Qian Peng,[c] Qianqian Li,[a] Zhen Li[a],*

[a]Department of Chemistry, Hubei Key Lab on Organic and Polymeric Opto-Electronic Materials, Wuhan University, Wuhan 430072, China.

[b]Department of Chemistry, Beijing Normal University, Beijing, 100875, P.R. China.

[c]Key Laboratory of Organic Solids, Beijing National Laboratory for Molecular Science (BNLMS), Institute of Chemistry, Chinese Academy of Sciences, 100190 Beijing, China.

Correspondence to: lizhen@whu.edu.cn or lichemlab@163.com.

Contents

1. General Information

Materials

Characterization

2. Figures and Tables

Fig. S1. The ^{1}H NMR spectrum of CAA.

Fig. S2. The ^{13}C NMR spectrum of CAA.

Fig. S3. The mass spectrum of CAA.

Fig. S4. (a) High-performance liquid chromatogram spectra of CAA, and MNA. (b) GC-MS of CAA.

Fig. S5. The PL behavior of CAA powder at room temperature.

Fig. S6. Lifetime decay profiles of fluorescent emission of the CAA.

Table S1. Photoluminescence properties of CAA crystal and powder.

Fig. S7. (a) Fluorescence and phosphorescence spectra of CAA crystal at 77 K; (b) Time-resolved measurement of low temperature phosphorescence at 489 nm from CAA crystal; (c) Photographs of CAA crystal taken at 77 K under 365 nm UV light or after ceasing the UV irradiation.

Fig. S8. (a) Fluorescence and phosphorescence spectra of CAA powder at 77 K; (b) Time-resolved measurement of low temperature phosphorescence at 489 nm from CAA powder; (c) Photographs of CAA powder taken at 77 K under 365 nm UV light or after ceasing the UV irradiation.

Fig. S9. (a) Fluorescence spectra of CAA in H_2O solutions at different concentrations (M) (λ_{ex}= 365 nm); (b) Absorption spectra of CAA in H_2O solutions at different concentrations; Photographs taken under 365 nm UV light of CAA in H_2O; (c) Fluorescence spectra of CAA in THF solutions at varying concentrations (M) (λ_{ex} = 365 nm); (d) Absorption spectra of CAA in THF solutions at different concentrations; Photographs taken under 365 nm UV light of CAA in THF.

Fig. S10. Lifetime decay profiles of fluorescent emission bands at 460 nm from CAA solution.

Table S2. Optical properties of CAA in H_2O solution.

Fig. S11. Excitation spectra of fluorescence emission of CAA in H_2O (at 460 nm) (a) and THF (at 450 nm) (b) solution.

Fig. S12. (a) Solid state UV-visible spectra; excitation (at 510 nm) spectra in phosphorescence mode and (b) PXRD patterns of CAA in different phases.

Fig. S13. (a) Fluorescence spectra of CAA in H_2O solutions at varying concentrations under 77 K and Phosphorescence spectra of CAA in H_2O solutions at varying concentrations under 77 K; (b) Time-resolved measurement from CAA in H_2O solutions at varying concentrations under 77 K. (c) Photographs of 1 M CAA/H_2O solution taken at 77 K under 365 nm UV light or after ceasing the UV irradiation.

Table S3. Phosphorescence lifetimes of CAA in H_2O solutions at varying concentrations under 77 K.

Table S4. Structure data of Cyanoacetic acid, Malononitrile and Malonic acid single crystals.

Fig. S14. Analyses of CAA crystal: (a) The interactions between two C≡N groups and two C=O of one layer; (b) The interactions between C≡N and C=O of two layers.

Table S5. The singlet and triplet excited state transition configurations of Isolated CAA revealed by TD-DFT calculations. The matched excited states that contain the same orbital transition components of S_1 and $|S_1\text{-}T_n| < 0.4$ eV were highlighted in red and 0.4 eV $< |S_1\text{-}T_n| < 0.6$ eV were highlighted in blue.

Table S6. The singlet and triplet excited state transition configurations of Coupled A in CAA revealed by TD-DFT calculations. The matched excited states that contain the same orbital

transition components of S_1 and $|S_1-T_n| < 0.4$ eV were highlighted in red and 0.4 eV $< |S_1-T_n| < 0.6$ eV were highlighted in blue.

Table S7. The singlet and triplet excited state transition configurations of Coupled B in CAA revealed by TD-DFT calculations. The matched excited states that contain the same orbital transition components of S_1 and $|S_1-T_n| < 0.4$ eV were highlighted in red and 0.4 eV $< |S_1-T_n| < 0.6$ eV were highlighted in blue.

Table S8. The singlet and triplet excited state transition configurations of Coupled C in CAA revealed by TD-DFT calculations. The matched excited states that contain the same orbital transition components of S_1 and $|S_1-T_n| < 0.4$ eV were highlighted in red and 0.4 eV $< |S_1-T_n| < 0.6$ eV were highlighted in blue.

Fig. S15. The Kohn-Sham frontier orbitals obtained from the Isolated, Coupled A, Coupled B and Coupled C in CAA.

Fig. S16. (a) Fluorescence spectrum and (b) phosphorescence spectrum of malonic acid crystal at room temperature.

Fig. S17. Fluorescence spectrum of 1 M malonic acid/H_2O solution.

Fig. S18. Time-resolved measurement of phosphorescence at 510 nm from malonic acid crystal at room temperature.

Fig. S19. (a) Fluorescence and phosphorescence spectra of MNA at 77 K; (b) Time-resolved measurement of low temperature phosphorescence at 509 nm from MNA; (c) Photographs of MNA taken at 77 K under 365 nm UV light or after ceasing the UV irradiation.

Fig. S20. Energy level diagrams of the Isolated MNA ($S_0 = 0$ eV).

Fig. S21. Energy level diagrams of the (a) Coupled H1 and (b) Coupled H2 for MNA ($S_0 = 0$ eV).

Table S9. The singlet and triplet excited state transition configurations of Isolated MNA revealed by TD-DFT calculations. The matched excited states that contain the same orbital transition components of S_1 and $|S_1-T_n| < 0.4$ eV were highlighted in red and 0.4 eV $< |S_1-T_n| < 0.6$ eV were highlighted in blue.

Table S10. The singlet and triplet excited state transition configurations of Coupled H1 revealed by TD-DFT calculations. The matched excited states that contain the same orbital transition components of S_1 and $|S_1-T_n| < 0.4$ eV were highlighted in red and 0.4 eV $< |S_1-T_n| < 0.6$ eV were highlighted in blue.

Table S11. The singlet and triplet excited state transition configurations of Coupled H2 revealed by TD-DFT calculations. The matched excited states that contain the same orbital transition components of S_1 and $|S_1\text{-}T_n| < 0.4$ eV were highlighted in red and 0.4 eV $< |S_1\text{-}T_n| < 0.6$ eV were highlighted in blue.

Fig. S22. The Kohn-Sham frontier orbitals obtained from the Isolated, Coupled H1, and Coupled H2 in MNA.

Fig. S23. (a) Fluorescence spectrum and (b) phosphorescence spectrum of malononitril crystal at room temperature.

Fig. S24. Fluorescence spectrum of 1 M malononitril/H_2O solution.

Fig. S25. (a) Fluorescence and phosphorescence spectra of MNN at 77 K; (b) Time-resolved measurement of low temperature phosphorescence at 529 nm from MNN; (c) Photographs of MNN taken at 77 K under 365 nm UV light or after ceasing the UV irradiation.

Table S12. The calculated spin orbital coupling (SOC) coefficient of MNN in different transition path by the configuration in crystal.

Fig. S26. The molecular structures and HOMO, LUMO orbitals obtained from the Isolated, Coupled CN1 and Coupled CN2 in MNN.

Fig. S27. (a) Fluorescence and phosphorescence spectra of methyl cyanoacetate at 77 K; (b) Time-resolved measurement of low temperature phosphorescence at 502 nm from methyl cyanoacetate; (c) Photographs of methyl cyanoacetate taken at 77 K under 365 nm UV light or after ceasing the UV irradiation.

Fig. S28. (a) Fluorescence and phosphorescence spectra of ethyl cyanoacetate at 77 K; (b) Time-resolved measurement of low temperature phosphorescence at 507 nm from ethyl cyanoacetate; (c) Photographs of ethyl cyanoacetate taken at 77 K under 365 nm UV light or after ceasing the UV irradiation.

Table S13. The calculated spin orbital coupling (SOC) coefficient of CAA in different transition path by the configuration in crystal.

Fig. S29. Energy level of CAA at S_1 minimum configuration.

Fig. S30. The transition route of CAA monomer. (a) vertical excitation (absorption); (b) radiative transition (fluorescence, F); (c) non-radiative transition; (d) intersystem crossing (ISC); (e) internal

conversion (IC); (f) triplet radiative transition (phosphorescence, P); (g) triplet non-radiative transition.

Fig. S31. The calculation model of a CAA layer, cutting from its single crystal (18 monomer).

Fig. S32. The energy level of CAA cluster in a layer of single crystal, three singlet states and ten triplet states were listed.

Table S14. The calculated spin orbital coupling (SOC) coefficient of MNA in different transition path by the configuration in crystal.

Fig. S33. The IR spectra of CAA, MNA and MNN in crystal and solution states.

3. Reference

Materials and Methods

Materials

H_2O was taken from ultrapure water systems. Tetrahydrofuran (THF) was treated to remove water and other possible impurities according to the literature.[1] Cyanoacetic acid was purchased from J&K SCIENTIFIC LTD. To avoid the influence of some unknown impurities, we purified CAA by chromatography on silica gel, followed by the recrystallization. In addition to the clean ^{1}H and ^{13}C NMR spectra, the results of elemental analysis and the high-performance liquid chromatogram spectra could confirm the purity of CAA. The single crystals of CAA were cultured from the mixtures of acetone and n-hexane. Malononitril (MNN) and malonic acid (MNA) were purchased from Sinopharm Chemical Reagent Co., Ltd and used directly.

Characterizations

^{1}H NMR and ^{13}C NMR spectra was recorded on a 400 MHz Varian Mercury, using D_2O as solvent. Mass spectrum was measured on a ZAB 3F-HF mass spectrophotometer. Elemental analyses of nitrogen, carbon and hydrogen were conducted on a Perkin-Elmer microanalyzer. High-performance liquid chromatogram spectra were recorded on a Agilent 1100, using 0.1% H_3PO_4 : acetonitrile (98:2 V/V) as mobile phase, the detection wavelength of CAA and MNA is 200 nm, 365 nm and 400 nm, the flow rate is 0.7 mL/min. UV-visible spectra were measured on a Shimadzu UV-2550. Gas Chromatography-Mass Spectra were measured on Varian 450-GC, Varian

320-MS. Photoluminescence spectra and phosphorescence lifetimes were performed on a Hitachi F-4600 fluorescence spectrophotometer. Fluorescence lifetimes were measured on a Quantaurus-Tau time-resolved spectrometer (Hamamatsu C11367-11). Photoluminescence quantum yields of CAA were determined with a HamamatsuC11347 Quantaurus-QY absolute fluorescence quantum yield spectrometer. Phosphorescence quantum yields were measured on a FLS980 spectrometer. The powder X-ray diffraction patterns were recorded by PANalytical X'Pert Pro with an X-ray source of Cu Kα ($\lambda = 1.5406$ Å) at a scan range of 5-50°. The single-crystal X-ray diffraction data of CAA, MNN and MNA crystals were collected in a Bruker APEX-II CCD diffractometer. The CCDC numbers of CAA, MNN and MNA are 1527812, 1829539 and 1528578, respectively. The CAA and MNN crystals were obtained from the acetone solvent, while the MNA crystal was obtained from dichloromethane solvent. The image of CAA crystal under visible light was taken by Leica M123 and Olympus IX71 research grade inverted microscope. The image of CAA crystal under UV illumination was taken by Olympus IX71 research grade inverted microscope.

CAA: A colorless crystal. ^{1}H-NMR (400 MHz, D_2O) δ (ppm): 3.412 (s, 2H). ^{13}C-NMR (100 MHz, D_2O) δ (ppm): 166.84, 115.05, 24.17. MS (ESI), m/z: 84.99, calcd for $C_3H_3NO_2$: 85.06. Elemental analyses for $C_3H_3NO_2$: C, 42.36; H, 3.55; N, 16.47. Found: C, 42.25; H, 3.75; N, 16.31.

The Gaussian 09 program was utilized to perform the TD-DFT calculations. The ground state (S_0) geometry was obtained from the single crystal structure and no further geometry optimization was conducted in order to maintain the specific molecular configuration and corresponding intermolecular locations. The exciton energies of the n-th singlet (S_n) and n-th triplet states (T_n) were obtained on the corresponding ground state structures using the TD-B3LYP/6-31G*. Kohn-Sham frontier orbital analyses and spin density distributions were obtained in order to elucidate the mechanisms of possible singlet-triplet intersystem crossings (ISC). The possible S_1 to T_n ISC channels are believed to share part of the same transition orbital compositions, and the energy levels of T_n are considered to lie within the range of $E_{S1} \pm 0.4$ eV.

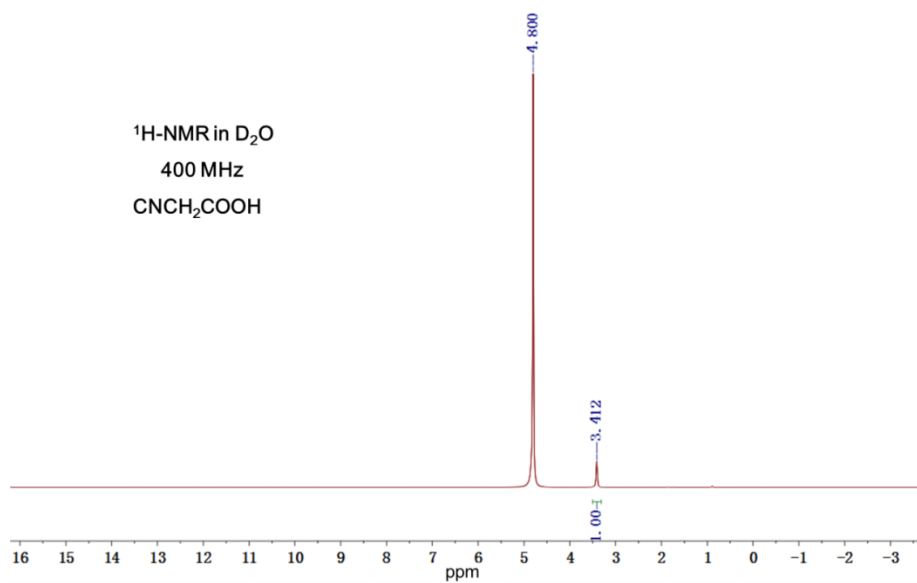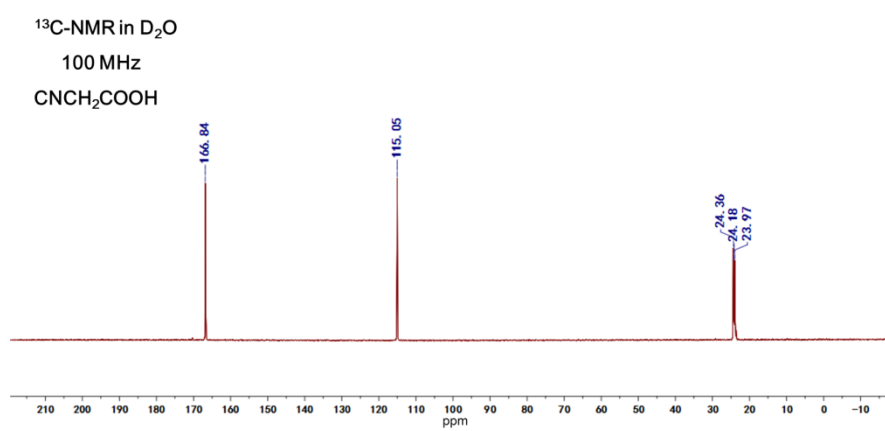**Fig. S1**. The ^{1}H NMR spectrum of CAA.

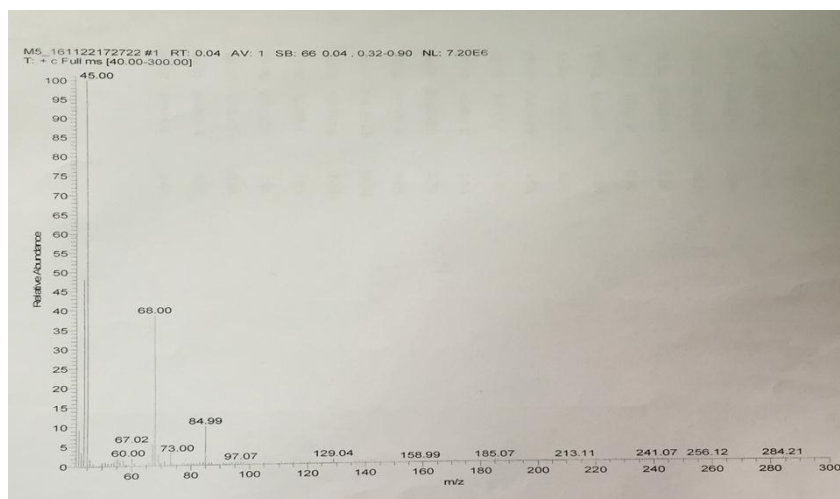**Fig. S2**. The ^{13}C NMR spectrum of CAA.
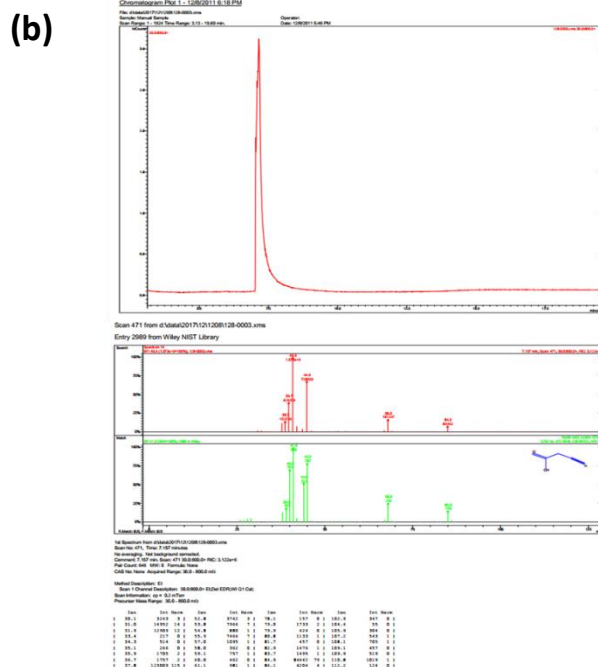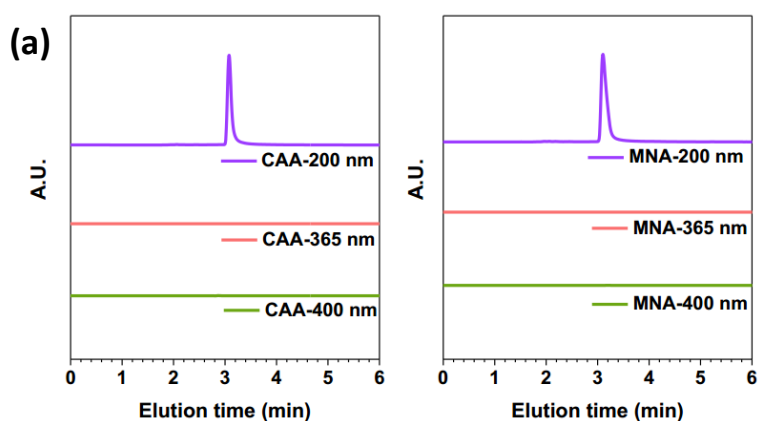
Fig. S3. The mass spectrum of CAA.

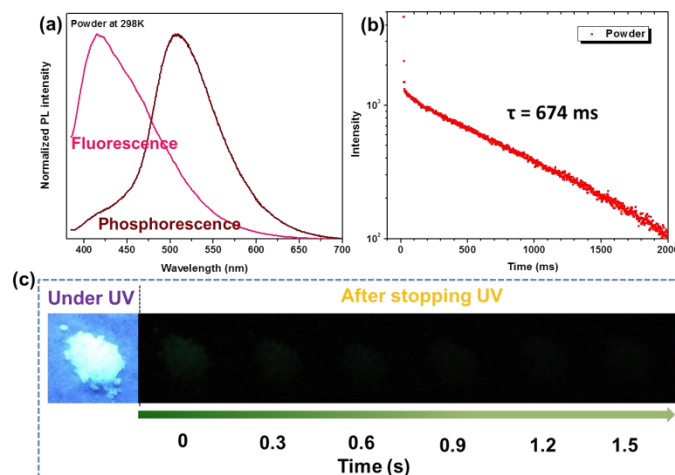**Fig. S4**. (a) High-performance liquid chromatogram spectra of CAA and MNA. (b) GC-MS of CAA.

Fig. S5. (a) Fluorescence and phosphorescence spectra of cyanoacetic acid (CAA) powder at room temperature; (b) Time-resolved measurement of phosphorescence at 506 nm from CAA powder; (c) Photographs of CAA powder taken at room temperature under 365 nm UV light or after ceasing the UV irradiation.
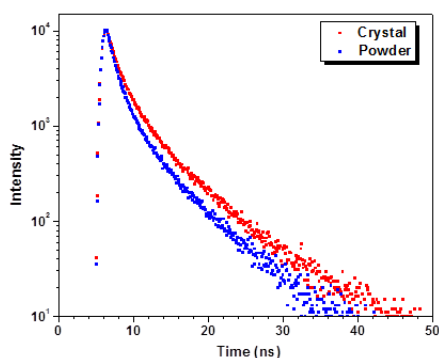
Fig. S6. Lifetime decay profiles of fluorescent emission bands (417 nm for crystal and 418 nm for powder) of CAA excited at 365 nm.

Table S1. Photoluminescence properties of CAA crystal and powder.

Compounds		$\lambda_{em,F}$ [nm]	$\lambda_{em,P}$ [nm]	Φ_F [%]	Φ_P [%]	τ_F [ns]	τ_P [ms]
CAA Crystal	300K	417	506	8.5	2.1	3.44	862
	77K	406	489	83.0	-	-	1385
CAA Powder	300K	418	506	7.6	1.8	2.68	674
	77K	407	489	57.7	-	-	1340

Fluorescence lifetimes experimental error: ± 0.0028 ns; phosphorescence lifetimes experimental error: ± 1ms; fluorescence quantum efficiencies experimental error: ± 5%; phosphorescence quantum efficiencies experimental error: ±0.4%.
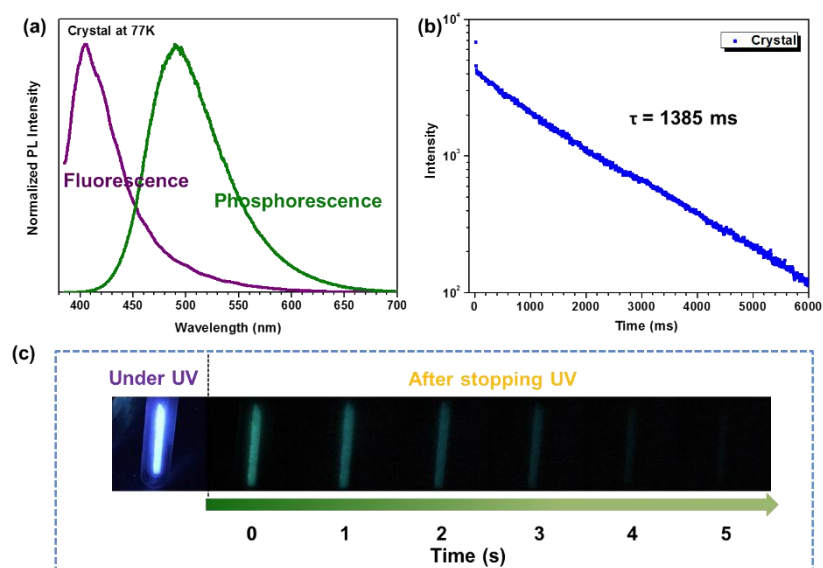
Fig. S7. (a) Fluorescence and phosphorescence spectra of CAA crystal at 77 K; (b) Time-resolved measurement of low temperature phosphorescence at 489 nm from CAA crystal; (c) Photographs of CAA crystal taken at 77 K under 365 nm UV light or after ceasing the UV irradiation.
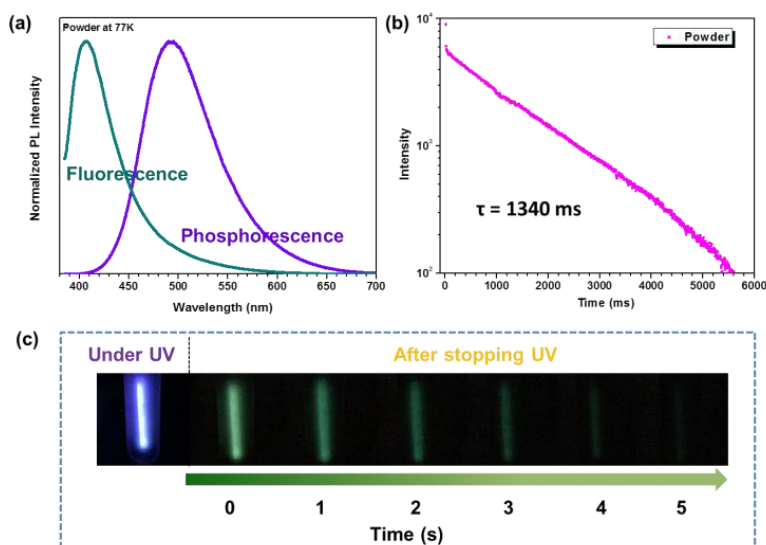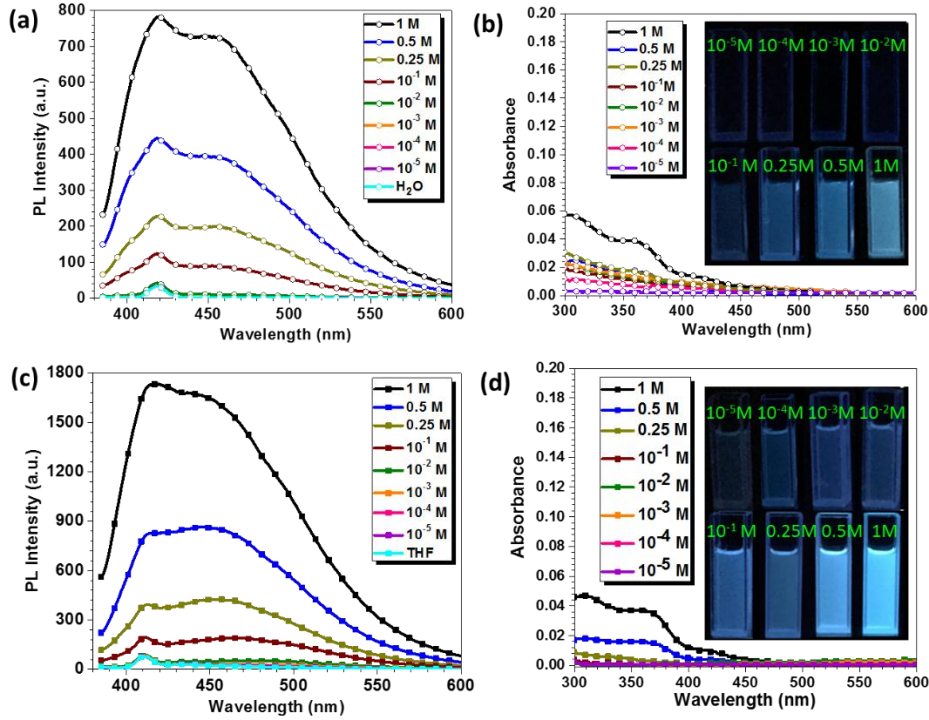

Fig. S8. (a) Fluorescence and phosphorescence spectra of CAA powder at 77 K; (b) Time-resolved measurement of low temperature phosphorescence at 489 nm from CAA powder; (c) Photographs of CAA powder taken at 77 K under 365 nm UV light or after ceasing the UV irradiation.

Fig. S9. (a) Fluorescence spectra of CAA in H_2O solutions at different concentrations (M) (λ_{ex}= 365 nm); (b) Absorption spectra of CAA in H_2O solutions at different concentr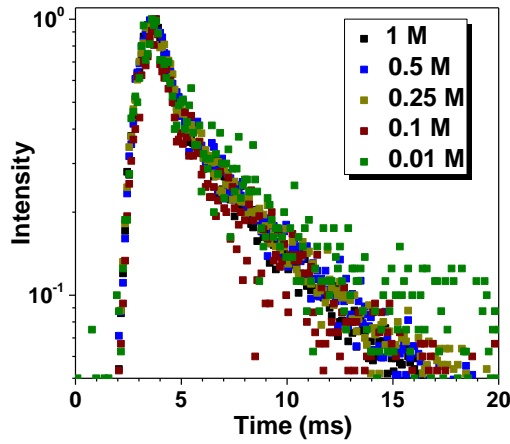ations; Photographs taken under 365 nm UV light of CAA in H_2O; (c) Fluorescence spectra of CAA in THF solutions at varying concentrations (M) (λ_{ex} = 365 nm); (d) Absorption spectra of CAA in THF solutions at different concentrations; Photographs taken under 365 nm UV light of CAA in THF.

Fig. S10. Lifetime decay profiles of fluorescent emission bands at 460 nm from CAA solution.

Table S2. Optical properties of CAA in H_2O solution.

Concentration of CAA in H_2O	λ_{max}^{em} [nm]	Φ_F [%]	τ [ns]	k_r [10^6 S^{-1}]	k_{nr} [10^8 S^{-1}]
1M	450	3.74	5.50	6.80	1.75
0.5M	447	2.94	5.41	5.43	1.79
0.25M	452	1.99	5.41	3.68	1.81
0.1M	452	0.03	4.88	0.06	2.00

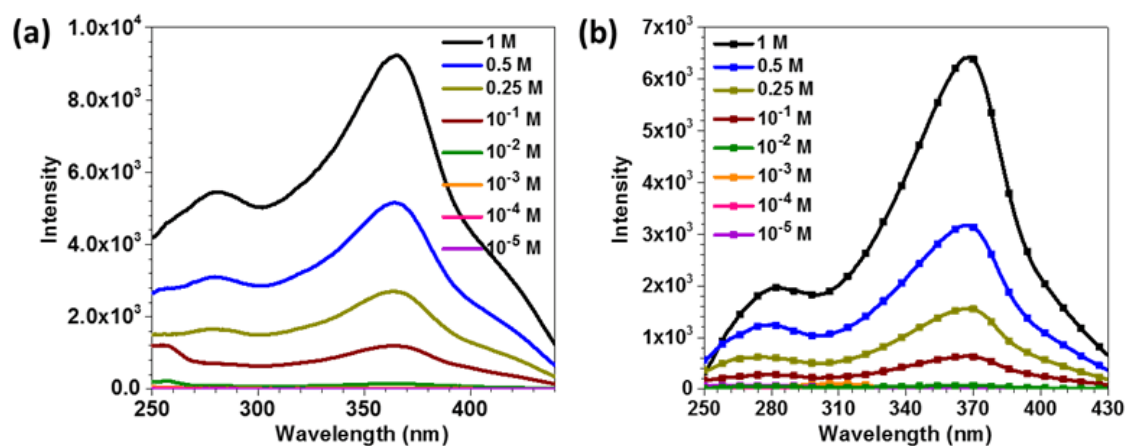$k_r = \Phi_F/\tau$, $k_{nr} = k_r/\Phi_F - k_r$

Fig. S11. Excitation spectra of fluorescence emission of CAA in H_2O (at 460 nm) (a) and THF (at 450 nm) (b) solution.
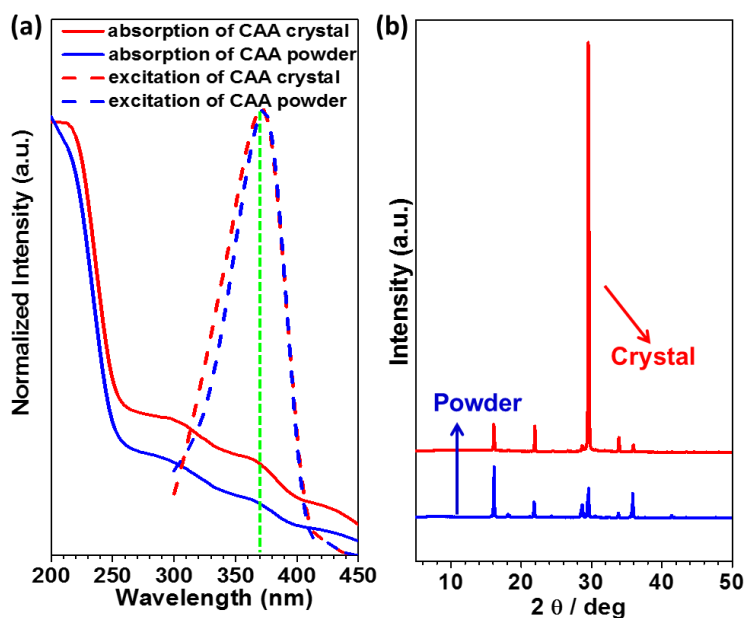

Fig. S12. (a) Solid state UV-visible spectra; excitation (at 510 nm) spectra in phosphorescence mode and (b) PXRD patterns of CAA in different phases.
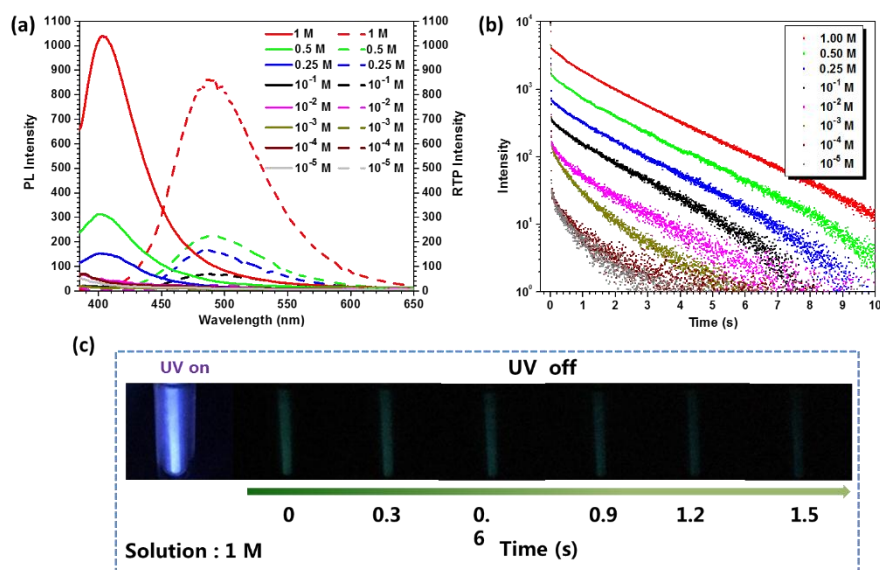
Fig. S13. (a) Fluorescence spectra of CAA in H_2O solutions at varying concentrations under 77 K and phosphorescence spectra of CAA in H_2O solutions at varying concentrations under 77 K; (b) Time-resolved measurement from CAA in H_2O solutions at varying concentrations under 77 K. (c) Photographs of 1 M CAA/H_2O solution taken at 77 K under 365 nm UV light or after ceasing the UV irradiation.

Table S3. Phosphorescence lifetimes of CAA in H_2O solutions at varying concentrations under 77 K.

C (Mol-1 L)	1.00	0.50	0.25	10^{-1}	10^{-2}
τ (ms)	1184	998	833	441	22.80

Table S4. Structure data of Cyanoacetic acid, Malononitrile and Malonic acid single crystals.

Name	Cyanoacetic acid	Malononitrile	Malonic acid
Empirical formula	C3H3N02	C3H2N2	C3H4O4
Formula weight	85.06	66.07	104.06
Wavelength (Å)	0.71073	0.71073	0.71073
Space group	Pnma	P21/c	P -1
a / Å	7.297 (4)	6.094 (5)	5.146 (3)
b / Å	6.045 (3)	7.560 (6)	5.331 (3)
c / Å	8.354 (4)	9.327 (6)	8.386 (6)
α / °	90	90	108.358 (10)
β / °	90	124.18 (4)	100.693 (13)
γ / °	90	90	95.005 (10)
volume / Å	368.5 (3)	355.5 (5)	211.9 (2)
Z	4	4	2
Dcalcd., g cm^{-3}	1.533	1.201	1.631
F(000)	176.0	136.0	108.0

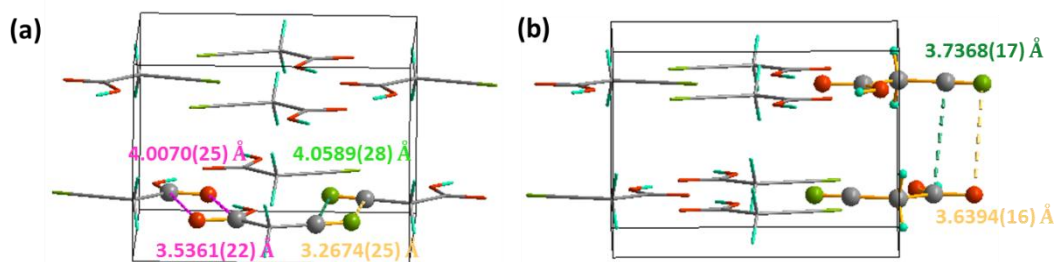| h_{max}, k_{max}, l_{max}	10,8,11	7,8,11	6,6,10
T_{min} , T_{max}	0.969, 0.974	0.983, 0.987	0.954, 0.959

Fig. S14. Analyses of CAA crystal: (a) The interactions between two C≡N groups and two C=O of one layer; (b) The interactions between C≡N and C=O of two layers.

Table S5. The singlet and triplet excited state transition configurations of Isolated CAA revealed by TD-DFT calculations. The matched excited states that contain the same orbital transition components of S_1 and $|S_1-T_n| < 0.4$ eV were highlighted in red and 0.4 eV $< |S_1-T_n| < 0.6$ eV were highlighted in blue.

Isolated	n-th	Energy (eV)	Transition configuration (%)
S_n	1	5.8913	H→L (97.6)
T_n	1	5.3255	H-2→L (2.3), H→L (96.7)
	2	5.8717	H-6→L (2.2), H-3→L (41.7), H-1→L (55.5)
	3	6.2560	H-3→L+2 (14.5), H-2→L+1 (45.3), H-1→L+2 (20.5), H→L+1 (17.5)
	4	7.0687	H-3→L+1 (21), H-2→L+2 (29.2), H-1→L+1 (33.7), H→L+2 (14.2)

Table S6. The singlet and triplet excited state transition configurations of Coupled A in CAA revealed by TD-DFT calculations. The matched excited states that contain the same orbital transition components of S_1 and $|S_1-T_n| < 0.4$ eV were highlighted in red and 0.4 eV $< |S_1-T_n| < 0.6$ eV were highlighted in blue.

Coupled A	n-th	Energy (eV)	Transition configuration (%)
S_n	1	5.9518	H→L (17.3), H→L+1 (78.3)
T_n	1	5.4331	H-4→L+1 (2.2), H→L (4.1), H→L+1 (91.9)
	2	5.6108	H-7→L (7.0), H-1→L (83.7), H→L (4.7)
	3	5.9051	H-12→L+1 (2.0), H-3→L+1 (24.1), H-2→L+1 (69.9)
	4	6.0693	H-9→ L (80.4), H-5→L (13.7)
	5	6.2524	H-8→L+2 (3.3), H-7→L+2 (32.5), H-5→L+3 (33.2), H-1→L+2 (26.5)
	6	6.2571	H-4→L+4 (44.6), H-3→L+5 (20.7), H-2→L+5 (14.1), H→L+4 (17.7)
	7	6.2740	H-1→L (4.9), H→L (90.9), H→L+1 (3.3)

	8	7.0662	H-9→L+2 (2.3), H-7→L+3 (19.6), H-5→L+2 (56.0), H-1→L+3 (17.0)

Table S7. The singlet and triplet excited state transition configurations of Coupled B in CAA revealed by TD-DFT calculations. The matched excited states that contain the same orbital transition components of S_1 and $|S_1$-$T_n| < 0.4$ eV were highlighted in red and 0.4 eV $< |S_1$-$T_n| < 0.6$ eV were highlighted in blue.

Coupled B	n-th	Energy (eV)	Transition configuration (%)
S_n	1	5.8974	H-1→L (97.2)
T_n	1	5.3356	H-1→L (96.5)
	2	5.3440	H-4→L+1 (2.4), H→L+1 (95.4),
	3	5.8452	H-13→L (2.3), H-6→L (9.6), H-3→L (86.9)
	4	5.9110	H-12→ L+1 (2.0), H-5→L+1 (44.6), H-2→L+1 (51.5)
	5	6.2382	H-8→L+2 (29.7), H-8→L+4 (5.1), H-6→L+3 (20.9), H-5→L+5 (2.1), H-4→L+2 (10.1), H-4→L+4 (3.4), H-3→L+3 (5.3), H-2→L+5 (3.3), H-1→L+2 (13.6), H→L+4 (2.4)
	6	6.2727	H-8→L+2 (9.6), H-6→L+3 (4.6), H-5→L+5 (10.8), H-4→L+2 (2.8), H-4→L+4 (32.0), H-2→L+5 (18), H-1→L+2 (2.4), H→L+2 (3.8), H→L+4 (10.9)
	7	7.0404	H-8→L+2 (11.5), H-6→L+3 (47.2), H-4→L+2 (2.6), H-3→L+3 (13.3), H-1→L+2 (17.9)

Table S8. The singlet and triplet excited state transition configurations of Coupled C in CAA revealed by TD-DFT calculations. The matched excited states that contain the same orbital transition components of S_1 and $|S_1$-$T_n| < 0.4$ eV were highlighted in red and 0.4 eV $< |S_1$-$T_n| < 0.6$ eV were highlighted in blue.

Coupled C	n-th	Energy (eV)	Transition configuration (%)
S_n	1	5.8462	H→L (17.3), H→L+1 (78.3)
T_n	1	5.2731	H-1→L+1 (44.5), H→L (52.7)
	2	5.2740	H-1→L (52.3), H→L+1 (44.9)
	3	5.8308	H-7→L+1 (9.7), H-6→L+1 (2.6), H-4→L (8.4), H-3 →L+1 (32.5), H-2→L (42.9)
	4	5.8326	H-7→ L (10.7), H-6→L (2.9), H-4→L+1 (7.7), H-3→L (36.7), H-2→L+1 (38.2)
	5	6.2720	H-7→L+2 (4.7), H-7→L+5 (7.6), H-6→L+2 (17.8), H-6→L+5 (2.2), H-5→L+3 (22.2), H-4→L+4 (9.7), H-3→L+5 (7.1), H-2→L+4 (4.5), H-1→L+3 (7.7), H→L+2 (9.4)
	6	6.2720	H-7→L+3 (4.3), H-7→L+4 (7.2), H-6→L+3 (18.4), H-5→L+2 (21.7), H-4→L+5 (10.7),

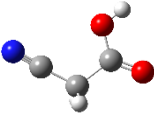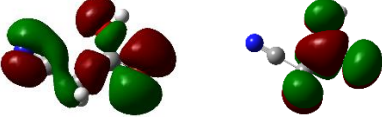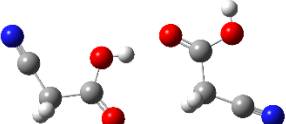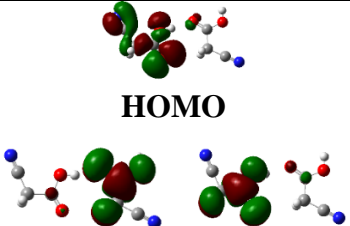|		
		H-3→L+4 (6.1), H-2→L+5 (5.2), H-1→L+2 (7.7), H→L+3 (9.3)
	7	7.0731	H-7→L+5 (16.6), H-6→L+2 (8.8), H-5→L+3 (9.1), H-4→L+4 (17.5), H-4→L+6 (2.5), H-3→L+5 (10.9), H-2→L+4 (7.9), H-1→L+3 (7.7), H→L+2 (6.9), H→L+5 (2.9)
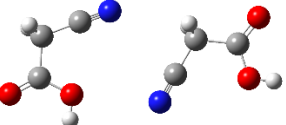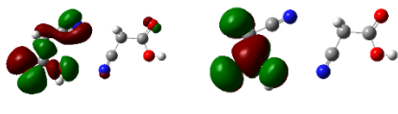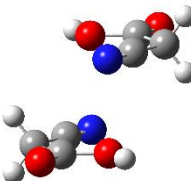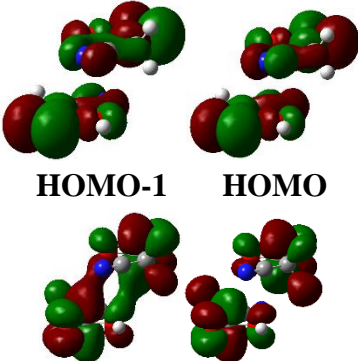
Isolated	$S_{1\,(H→L)}→T_{1(H→L)}$	**HOMO** **LUMO**
Coupled A	$S_{1(H→L,\ H→L+1)}→T_{1(H→L,\ H→L+1)}$ $S_{1(H→L,\ H→L+1)}→T_{2\ (H→L)}$ $S_{1(H→L,\ H→L+1)}→T_{7(H→L,\ H→L+1)}$	**HOMO** **LUMO** **LUMO+1**
Coupled B	$S_{1(H-1→L)}→T_{1(H-1→L)}$	**HOMO-1** **LUMO**
Coupled C	$S_{1(H-1→L,H→L+1)}→T_{2(H-1→L,\ H→L+1)}$	**HOMO-1** **HOMO** **LUMO** **LUMO+1**

Fig. S15. The Kohn-Sham frontier orbitals obtained from the Isolated, Coupled A, Coupled B and Coupled C in CAA.
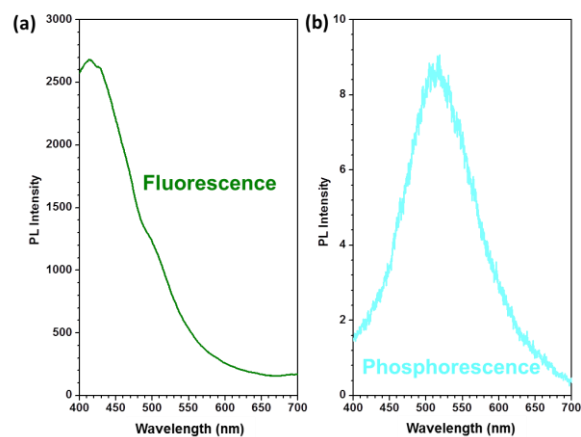
Fig. S16. (a) Fluorescence spectrum and (b) phosphorescence spectrum of malonic acid crystal at room temperature.
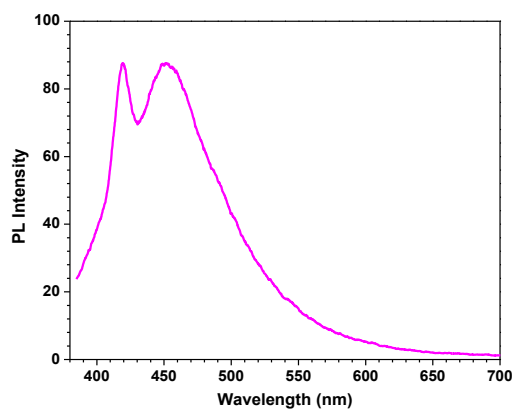

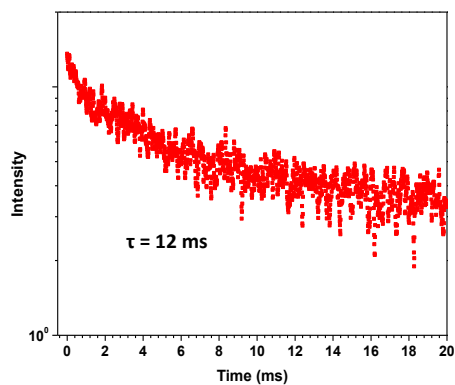**Fig. S17.** Fluorescence spectrum of 1 M malonic acid/H_2O solution.

Fig. S18. Time-resolved measurement of phosphorescence at 510 nm from malonic acid crystal at room temperature.
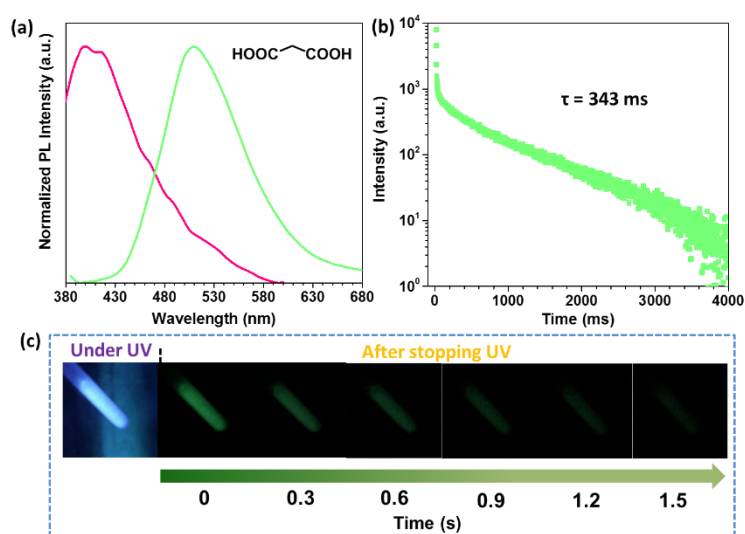
Fig. S19. (a) Fluorescence and phosphorescence spectra of MNA at 77 K; (b) Time-resolved measurement of low temperature phosphorescence at 509 nm from MNA; (c) Photographs of MNA taken at 77 K under 365 nm UV light or after ceasing the UV irradiation.
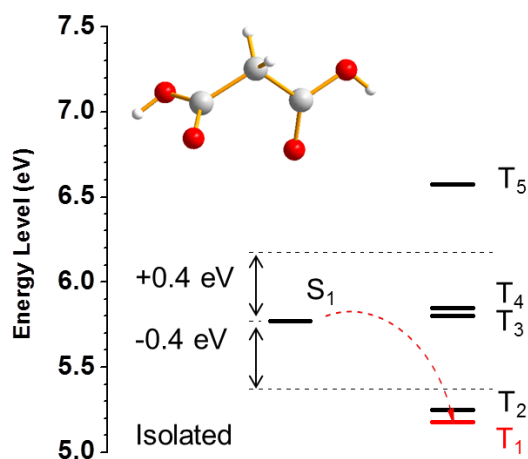

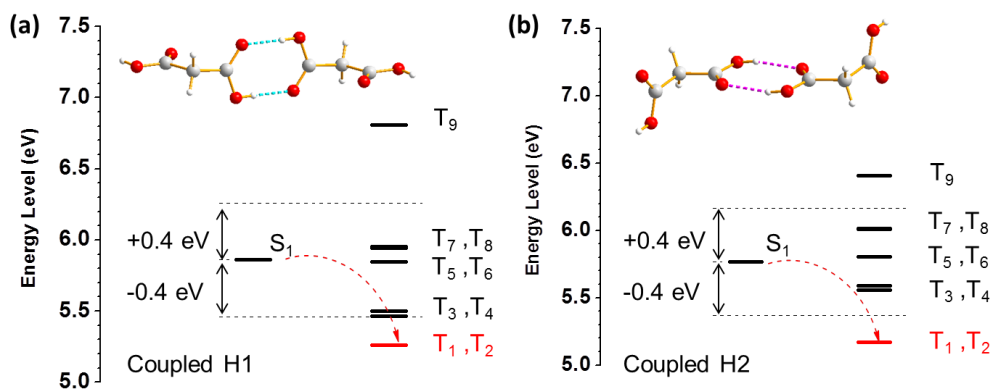**Fig. S20**. Energy level diagrams of the Isolated MNA ($S_0 = 0$ eV).

Fig. S21. Energy level diagrams of the (a) Coupled H1 and (b) Coupled H2 for MNA ($S_0 = 0$ eV).

Table S9. The singlet and triplet excited state transition configurations of Isolated MNA revealed by TD-DFT calculations. The matched excited states that contain the same orbital transition components of S_1 and $|S_1-T_n| < 0.4$ eV were highlighted in red and 0.4 eV $< |S_1-T_n| < 0.6$ eV were highlighted in blue.

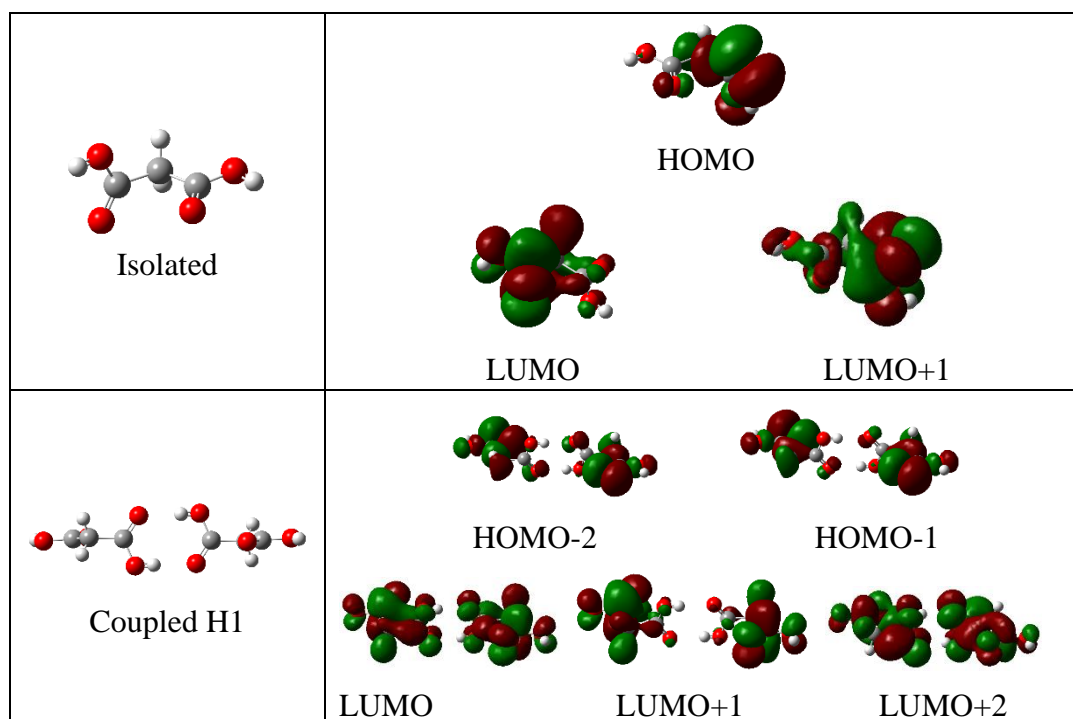| Isaolated	n-th	Energy (eV)	Transition configuration (%)
S_n	1	5.7730	H→L (5.1), H→L+1 (93.7)
T_n	1	5.1787	H→L (3.6), H→L+1 (94.9)
	2	5.2531	H-1→L (95.5), H-1→L+1 (2.2)
	3	5.8020	H-3→L (2.2), H-3→L+1 (7.3), H-2→L (6.0), H-2→L+1 (81.7)
	4	5.8468	H-3→L (81.7), H-2→L (8.4), H-2→L+1 (6.4)
	5	6.5710	H→ L(93.7), H→L+1 (3.5)

Table S10. The singlet and triplet excited state transition configurations of Coupled H1 revealed by TD-DFT calculations. The matched excited states that contain the same orbital transition components of S_1 and $|S_1-T_n| < 0.4$ eV were highlighted in red and 0.4 eV $< |S_1-T_n| < 0.6$ eV were highlighted in blue.

Coupled H1	n-th	Energy (eV)	Transition configuration (%)
S_n	1	5.8605	H-2→L (22.3), H-2→L+1 (17.7), H-2→L+2 (6.3), H-1→L (16.8), H-1→L+1 (28.1), H-1→L+2 (4.5)
T_n	1	5.2606	H-2→L (18.9), H-2→L+1 (22.1), H-2→L+2 (5.5), H-1→L (20.1), H-1→L+1 (23.6), H-1→L+2 (5.7)
	2	5.2613	H-2→L (17.8), H-2→L+1 (24.7), H-2→L+2 (5.7), H-1→L (17.7), H-1→L+1 (24.4), H-1→L+2 (5.6)
	3	5.4658	H-3→L+2 (31.4), H→L (16.7), H→L+2 (47.6)
	4	5.4988	H-3→L (10.1), H-3→L+2 (29.1), H→L+3 (55.6)
	5	5.8461	H-7→L (12.0), H-7→L+1 (15.9), H-7→L+2 (4.3), H-6→L (17.4), H-6→L+1 (19.3), H-6→L+2 (5.8), H-5→L (6.6), H-5→L+1 (7.8), H-4→L (3.2), H-4→L+1 (2.9)
	6	5.8473	H-7→L (12.2), H-7→L+1 (16.1), H-7→L+2 (4.8), H-6→L (14.3), H-6→L+1 (22.1), H-6→L+2 (5.2), H-5→L (6.6), H-5→L+1 (7.7), H-4→L (2.7), H-4→L+1 (3.4)
	7	5.9446	H-7→L+3 (8.7), H-5→L+3 (31.7), H-4→L (12.2), H-4→L+2 (39.1)
	8	5.9545	H-7→L (4.0), H-7→L+2 (6.6), H-6→L+3 (2.7), H-5→L (7.9), H-5→L+2 (28.0), H-4→L+3 (45.7)
	9	6.8087	H-2→L (5.4), H-2→L+2 (15.6), H-2→L+3

| | | | (22.5), H-1→L+2 (28.3), H-1→L+3 (13.9) |

Table S11. The singlet and triplet excited state transition configurations of Coupled H2 revealed by TD-DFT calculations. The matched excited states that contain the same orbital transition components of S_1 and $|S_1\text{-}T_n| < 0.4$ eV were highlighted in red and 0.4 eV $< |S_1\text{-}T_n| < 0.6$ eV were highlighted in blue.

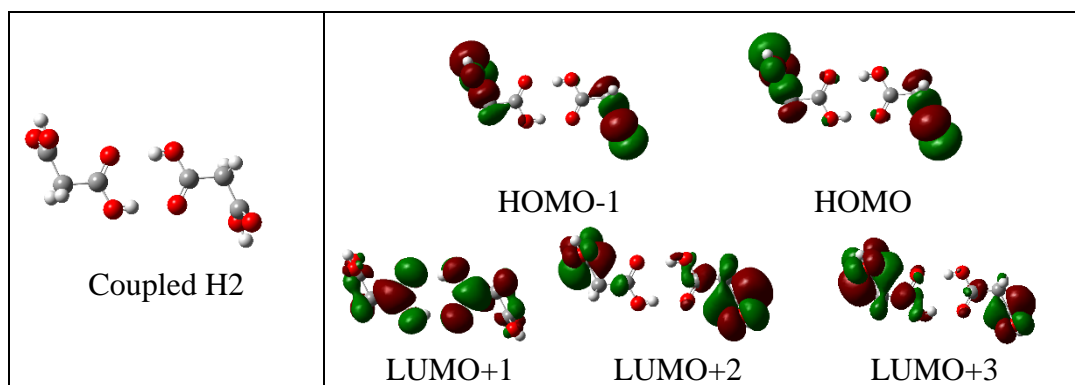| Coupled H2	n-th	Energy (eV)	Transition configuration (%)
S_n	1	5.7663	H-1→L+1 (2.2), H-1→L+2 (22.5), H-1→L+3 (23.2), H→L+2 (48.5)
T_n	1	5.1707	H-1→L+2 (37.2), H-1→L+3 (9.3), H→H+2 (39.3), H→H+3 (11.3)
	2	5.1714	H-1→L+2 (10.8), H-1→L+3 (39.8), H→L+2 (11.0), H→L+3 (35.6)
	3	5.5592	H-3→L+1 (32.6), H-2→L (64.5)
	4	5.5875	H-3→L (39.9), H-2→L+1 (56.5)
	5	5.8024	H-5→L+2 (34.4), H-5→L+3 (9.6), H-4→L+2 (37.6), H-4→L+3 (9.7)
	6	5.8035	H-5→L+2 (10.9), H-5→L+3 (36.0), H-4→L+2 (9.7), H-4→L+3 (34.8)
	7	6.0085	H-7→L+1 (38.2), H-6→L (49.1), H-4→L (4.4)
	8	6.0168	H-7→L (43.2), H-6→L+1 (44.1), H-5→L (2.2), H-4→L+1 (3.7)
	9	6.4061	H-1→L+1 (33.3), H→L (60.9)

Fig. S22. The Kohn-Sham frontier orbitals obtained from the Isolated, Coupled H1, and Coupled H2 in MNA.
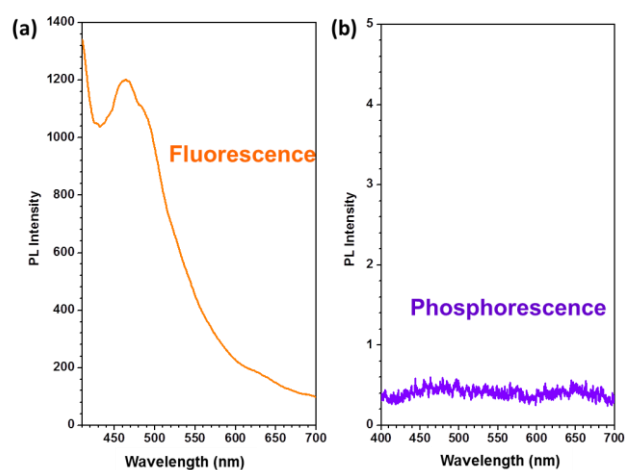

Fig. S23. (a) Fluorescence spectrum and (b) phosphorescence spectrum of malononitril crystal at room temperature.
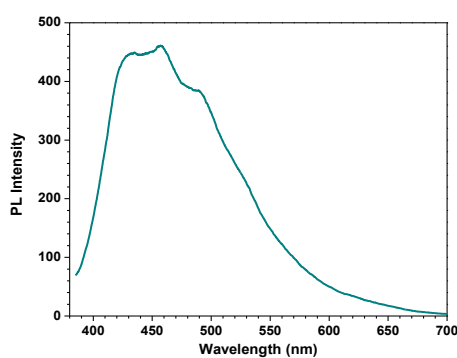

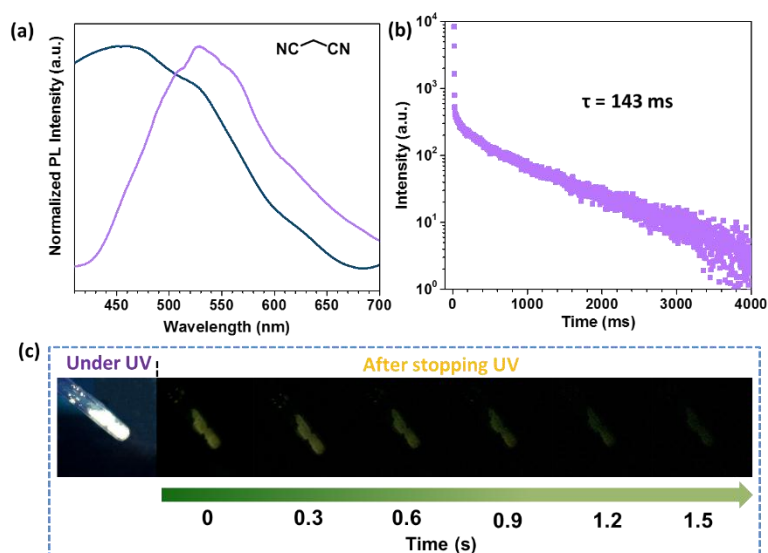**Fig. S24.** Fluorescence spectrum of 1 M malononitril/H_2O solution.

Fig. S25. (a) Fluorescence and phosphorescence spectra of MNN at 77 K; (b) Time-resolved measurement of low temperature phosphorescence at 529 nm from MNN; (c) Photographs of MNN taken at 77 K under 365 nm UV light or after ceasing the UV irradiation.

Table S12. The calculated spin orbital coupling (SOC) coefficient of MNN in different transition path by the configuration in crystal.

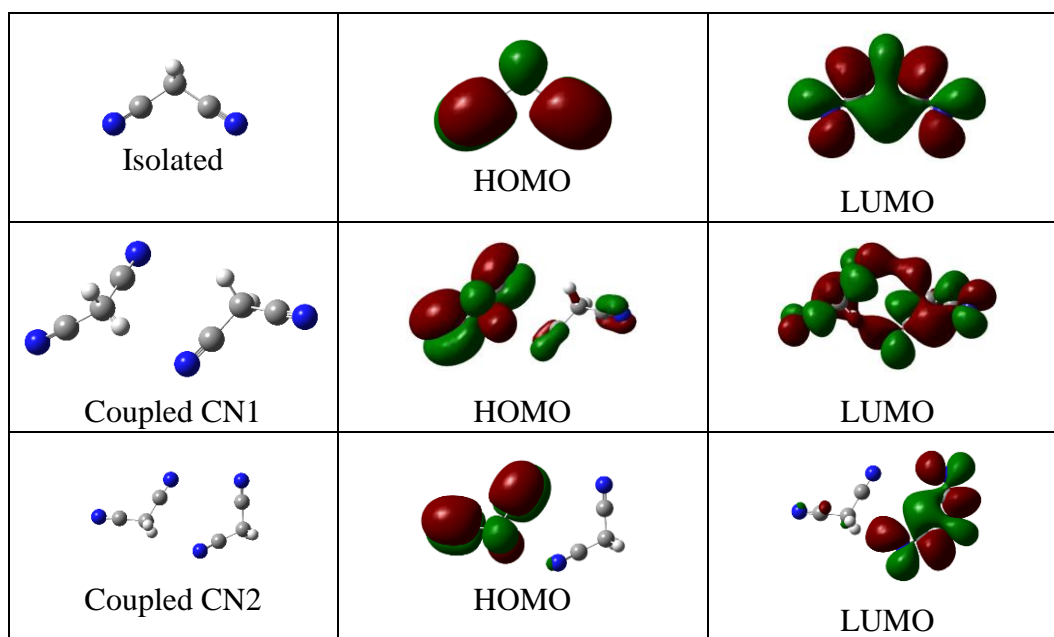| Transition	SOC	Transition	SOC
$S_0 \rightarrow T_1$	1.188	$S_1 \rightarrow T_1$	2.763
$S_0 \rightarrow T_2$	1.512	$S_1 \rightarrow T_2$	2.387
$S_0 \rightarrow T_3$	3.411	$S_1 \rightarrow T_3$	0.123

Fig. S26. The molecular structures and HOMO, LUMO orbitals obtained from the Isolated, Coupled CN1 and Coupled CN2 in MNN.
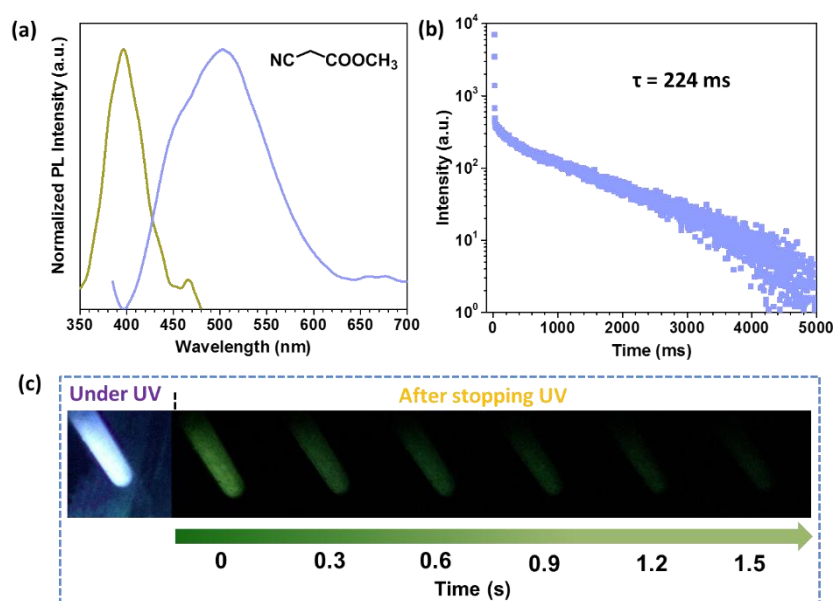
Fig. S27. (a) Fluorescence and phosphorescence spectra of methyl cyanoacetate at 77 K; (b) Time-resolved measurement of low temperature phosphorescence at 502 nm from methyl cyanoacetate; (c) Photographs of methyl cyanoacetate taken at 77 K under 365 nm UV light or after ceasing the UV irradiation.
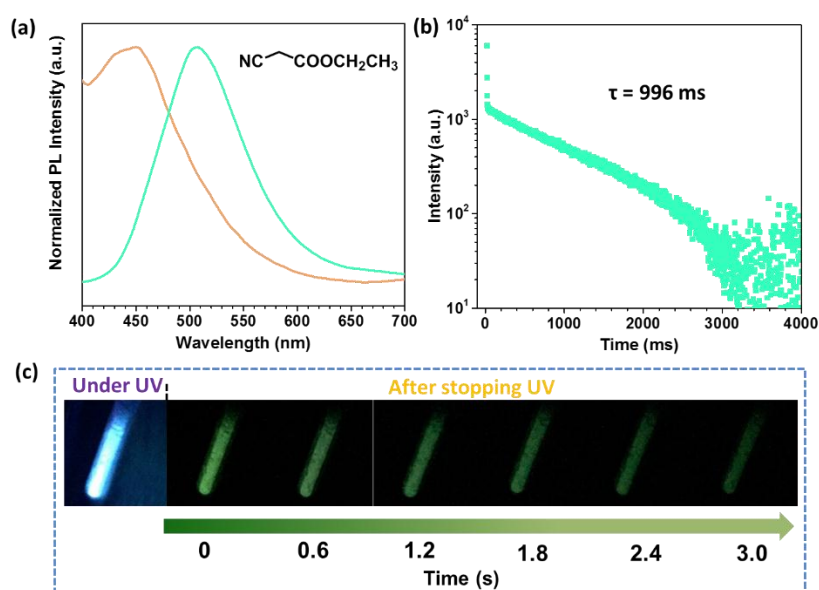

Fig. S28. (a) Fluorescence and phosphorescence spectra of ethyl cyanoacetate at 77 K; (b) Time-resolved measurement of low temperature phosphorescence at 507 nm from ethyl cyanoacetate; (c) Photographs of ethyl cyanoacetate taken at 77 K under 365 nm UV light or after ceasing the UV irradiation.

Other attempts for theory calculation

The spin orbital coupling (SOC) calculations were carried out at the TD/b3lyp /6-31g* level using the BDF program package[2], and the transition rates including radiative, non-radiative, intersystem crossing were carried out by MOMAP program package[3]. The molecular geometry optimization and frequency calculation for the ground state (S_0) and the first triplet state (T_1) were performed at b3lyp/6-31g* level, and for the first excited singlet state (S_1) was at the TD/b3lyp/6-31g* level, these calculations were carried out with Gaussian 09 program[4].
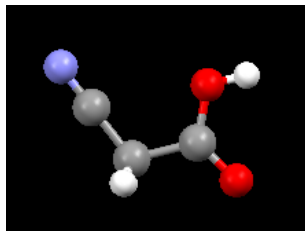

Table S13. The calculated spin orbital coupling (SOC) coefficient of CAA in different transition path by the configuration in crystal.

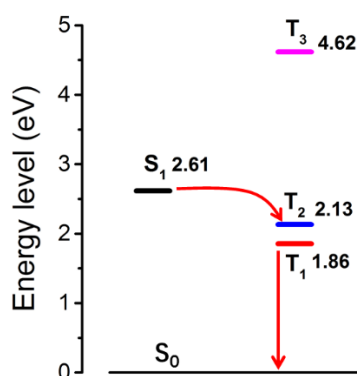| Transition	SOC	Transition	SOC
$S_0 \rightarrow T_1$	**31.657**	$S_1 \rightarrow T_1$	0.079
$S_0 \rightarrow T_2$	0.039	$S_1 \rightarrow T_2$	**23.639**
$S_0 \rightarrow T_3$	0.059	$S_1 \rightarrow T_3$	0.730

Fig. S29. Energy level of CAA at S_1 minimum configuration.

The calculated SOC coefficient revealed that the most intense SOC effect happened in the transition of $S_0 \rightarrow T_1$ (31.657) and $S_1 \rightarrow T_2$ (23.639). The SOC coefficient varies little at different nuclear configuration of S_0, S_1 and T_1, thus, the values in Table 1 could be considered as constant. The energy level diagram of CAA at S_1 minimum configuration was presented in Fig. S29.

The intersystem crossing rate is proportional to the division of $<SOC/\Delta E_{S-T}>$. The transition of $S_1 \rightarrow T_3$ can be ruled out because of much too high energy gap. With these considerations, the most likely transition route of phosphorescence production would be from $S_1 \rightarrow T_2$, then $T_2 \rightarrow T_1$ through internal conversion, which follow the kasha's rule, at last, $T_1 \rightarrow S_0$ transition gives rise of phosphorescence. According to this suspicion, we calculated transition rate of CAA monomer in detail.
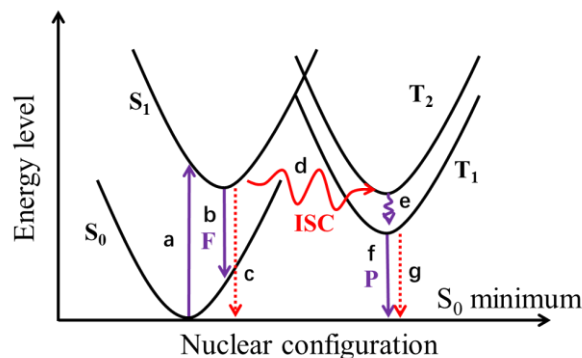
Fig. S30. The transition route of CAA monomer. (a) vertical excitation (absorption); (b) radiative transition (fluorescence, F); (c) non-radiative transition; (d) intersystem crossing (ISC); (e) internal conversion (IC); (f) triplet radiative transition (phosphorescence, P); (g) triplet non-radiative transition.

The detailed transition routes were presented in Fig. S29, and the corresponding calculated transition rates were listed as below:

$K_{r,F}(S_1 \rightarrow S_0) = 3.02 \times 10^5 \ s^{-1}$

$K_{nr,F}(S_1 \rightarrow S_0) = 1.51 \times 10^8 \ s^{-1}$

$K_{isc}(S_1 \rightarrow T_1) = 1.94 \times 10^5 \ s^{-1}$

$K_{isc}(S_1 \rightarrow T_2) = 2.55 \times 10^{10} \ s^{-1}$

$K_{r,P}(T_1 \rightarrow S_0) = 1.58 \times 10^9 \ s^{-1}$

$K_{nr,P}(T_1 \rightarrow S_0) = 2.52 \times 10^{10} \ s^{-1}$

The value of $K_{nr,F}$ is three magnitude higher than that of $K_{r,F}$, meaning that CAA monomer was non-fluorescent. Although the values of $K_{isc}(S_1 \rightarrow T_1)$, $K_{isc}(S_1 \rightarrow T_2)$ and $K_{r,P}(T_1 \rightarrow S_0)$ involving spin flip between singlet and triplet states, might be systemically larger than those without SOC effect, the transition rate of $S_1 \rightarrow T_1$ is negligible when compared with $S_1 \rightarrow T_2$. Therefore, the triplet exciton should be produced at T_2 state, then falling to T_1 state through the internal conversion process. As for the dissipating rate of triplet exciton ($T_1 \rightarrow S_0$), the much intense $K_{nr,P}$ than $K_{r,P}$ indicated that single CAA molecule would not emit phosphorescence.

According to the above analysis, it could be deduced that single CAA molecule has potential to emit phosphorescence, but the strong non-radiative transition dissipates the exciton energy, causing its non-luminescence. While CAA in crystal state or at 77 K, the aggregate effect (mainly from hydrogen bonding) or low temperature could depress the non-radiative transition rate on large extent. Thus, correspondingly, its RTP and low temperature phosphorescence were understandable.
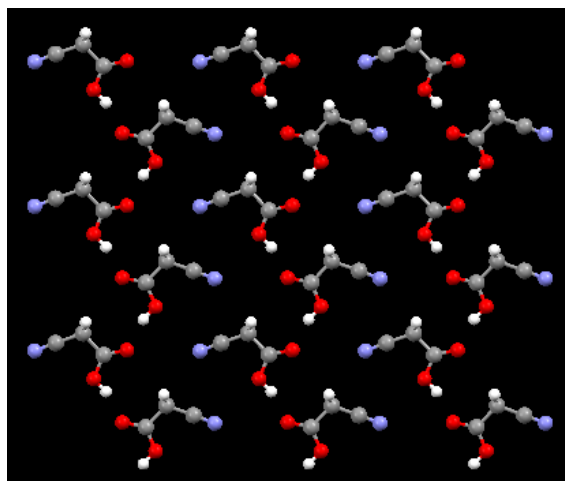
Fig. S31. The calculation model of a CAA layer, cutting from its single crystal (18 monomer).
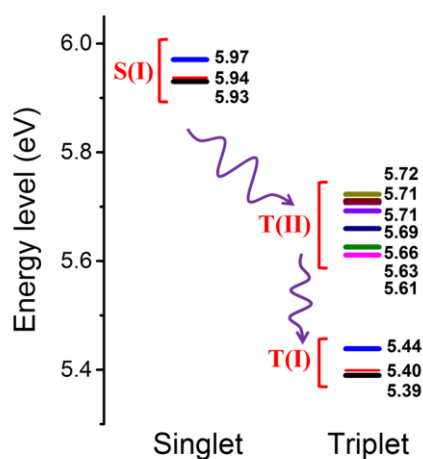

Fig. S32. The energy level of CAA cluster in a layer of single crystal, three singlet states and ten triplet states were listed.

To further study the energy level distribution of CAA cluster in a layer of single crystal, we built calculation model composed of 18 monomers (Fig. S30) and listed three singlet states and ten triplet states in Fig. S31. The TD-DFT calculation results revealed that energy levels were degenerated on large extent, which could be roughly divided into S(Ⅰ), T(Ⅰ) and T(Ⅱ). Thus, the energy gap between singlet and triplet decreased on a large scale, and the transition path was similar to that of monomer to some extent, from S(Ⅰ) to T(Ⅱ) through ISC process, then to T(Ⅰ), at last to S_0, accompanying with the phosphorescence emission.

Table S14. The calculated spin orbital coupling (SOC) coefficient of MNA in different transition path by the configuration in crystal.

Transition	SOC	Transition	SOC
$S_0 \rightarrow T_1$	**31.296**	$S_1 \rightarrow T_1$	0.544
$S_0 \rightarrow T_2$	**32.376**	$S_1 \rightarrow T_2$	0.201
$S_0 \rightarrow T_3$	0.708	$S_1 \rightarrow T_3$	**24.396**

Additional proofs for hydrogen bonds

We also investigated the hydrogen bonds of these compounds by IR spectra of CAA, MNA, MNN in crystals and H_2O solutions with different concentrations (10^{-5}, 10^{-3} and 1 M), according to the literature[5]. As shown in Fig. S33, some new and strong IR peaks around 2500∼3000 cm^{-1} appeared in the CAA and MNA crystals in comparison with their corresponding H_2O solutions, and these broad and loose peaks represent the O-H stretching vibrations of carboxyl dimers, suggesting the formation of strong intermolecular hydrogen bonds in crystals. As for compound MNN, no obvious peaks for associated complexes could be observed as the result of the weak intermolecular hydrogen bonds. Thus, the changes of IR spectra from solutions to crystals could well demonstrate the formation of strong intermolecular bonds in CAA and MNA crystals
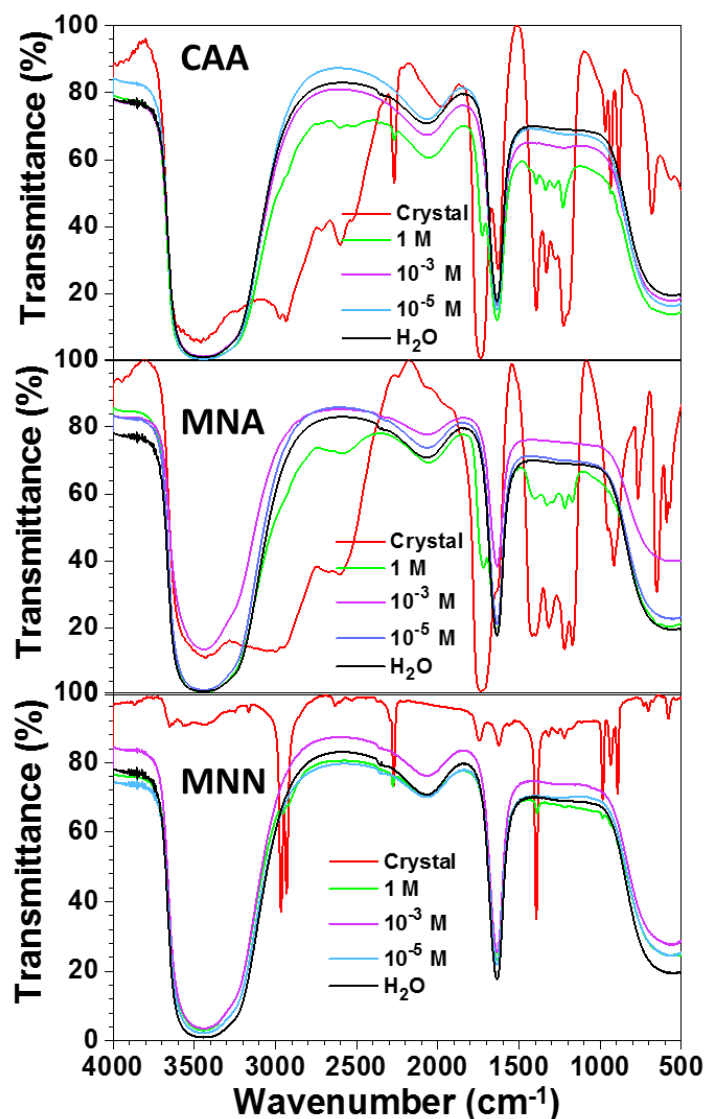

Fig. S33 The IR spectra of CAA, MNA and MNN in crystal and solution states.

Reference

(1) H. Li, Y. Hou, Y. Yang, R. Tang, J. Chen, H. Wang, H. Han, T. Peng, Q. Li, Z. Li, *ACS Appl. Mat. Interfaces*, 2013, **5**, 12469.

(2) W. J. Liu, F. Wang, L. M. Li, J. *Theor. Comput. Chem.*, 2003, **2**, 257.

(3) Z. G. Shuai, Q. Peng, Y. L. Niu, H. Geng, MOMAP, a molecular materials property

prediction package, revision 0.2.004; Tsinghua University: Beijing, China, 2014. http://www.shuaigroup.net/.

(4) M. J. Frisch, G. W. Trucks, H. B. Schlegel, G. E. Scuseria, M. A. Robb, J. R. Cheeseman, G. Scalmani, V. Barone, B. Mennucci, G. A. Petersson, H. Nakatsuji, M. Caricato, X. Li, H. P. Hratchian, A. F. Izmaylov, J. Bloino, G. Zheng, J. L. Sonnenberg, M. Hada, M. Ehara, K. Toyota, R. Fukuda, J. Hasegawa, M. Ishida, T. Nakajima, Y. Honda, O. Kitao, H. Nakai, T. Vreven, J. A. Montgomery, Jr., J. E. Peralta, F. Ogliaro, M. Bearpark, J. J. Heyd, E. Brothers, K. N. Kudin, V. N. Staroverov, T. Keith, R. Kobayashi, J. Normand, K. Raghavachari, A. Rendell, J. C. Burant, S. S. Iyengar, J. Tomasi, M. Cossi, N. Rega, J. M. Millam, M. Klene, J. E. Knox, J. B. Cross, V. Bakken, C. Adamo, J. Jaramillo, R. Gomperts, R. E. Stratmann, O. Yazyev, A. J. Austin, R. Cammi, C. Pomelli, J. W. Ochterski, R. L. Martin, K. Morokuma, V. G. Zakrzewski, G. A. Voth, P. Salvador, J. J. Dannenberg, S. Dapprich, A. D. Daniels, O. Farkas, J. B. Foresman, J. V. Ortiz, J. Cioslowski, and D. J. Fox, Gaussian, Inc., Wallingford CT, 2013.

(5) S. Saha, G. R. Desiraju, *J. Am. Chem. Soc.*, 2018, **140**, 6361.